Applied Thermal Engineering 230 (2023) 120754

Contents lists available at ScienceDirect

Applied Thermal Engineering

journal homepage: www.elsevier.com/locate/ate

Research Paper

Numerical and experimental evaluation of the passive pre-chamber concept for future CNG SI engines

R. Payri *, R. Novella, I. Barbery, O. Bori-Fabra

CMT – Motores Térmicos, Universitat Politècnica de València, Camino de Vera, 46022 Valencia, Spain

ARTICLE INFO

Keywords:
Spark ignition engines
Passive pre-chamber
CNG
CFD combustion modeling
EGR
WLTP driving-cycle simulations

ABSTRACT

The third decade of the 21st century is set to be one of the most relevant in terms of the transition of methods and forms of using different energy sources, with short and medium-term developments on the road to decarbonization. One of the most widely accepted measures on this path is the reduction of CO_2 emissions from internal combustion engines, which is why different concepts are being studied in order to optimize combustion. Furthermore, this research focuses on developing a suitable Spark-Ignition (SI) engine configuration integrating the passive pre-chamber ignition concept (TJI), together with a high compression ratio and the use of the Miller cycle, in order to exploit the benefits of using Compressed Natural Gas (CNG) as fuel. Thus, the novelty of this investigation is the detailed evaluation of the aforementioned SI engine architecture by state-of-the-art CFD simulations and a broad experimental campaign, to understand the advantages of the combined technologies against a conventional SI engine operating with gasoline. The pre-chamber technology is able to overcome the issues associated with the lower laminar flame speeds of CNG, and the reduction of turbulence caused by prematurely closing the intake valve with the Miller cycle. The experimental results showed that the new engine definition achieved higher levels of indicated efficiency compared to the baseline engine (around a 3% increase at high load/speed conditions). Moreover, the addition of EGR allows to further improve the engine performance, extending the load limit in the low-end torque region of the engine map. Finally, a full dynamic 1D model of a current passenger car vehicle was developed to perform transient driving cycle simulations, showing a reduction of 15% in fuel consumption and 25% in CO_2 emissions for the new engine definition compared to the baseline engine.

1. Introduction

Society in the first half of the 21st century faces unprecedented challenges that will determine its future. Most of these challenges are related to energy production, in which fossil fuels take a big part, contributing to impact on global warming and pollution. Over 25% of the energy produced worldwide is destined to be consumed in the transportation sector [1]. In addition, this sector is also responsible of emitting a high percentage of Carbon Dioxide (CO_2) and hazardous pollutants like Carbon Monoxide (CO) and Nitrogen Oxides (NO_x), particularly in road transportation which accounts for 70% of these emissions [2,3]. Consequently, there is a flourishing of new global treaties due to the awareness of governments in terms of reducing the carbon footprint in this sector, focusing on implementing restrictions on emissions. Therefore, engine manufacturers are being obligated to develop modern powertrains that are able to comply with the new emissions restrictions, without compromising significantly the global performance of the vehicle. In order to achieve these requirements, the combination of modern technologies and the development of new ones, for improving the engine thermal efficiency and reducing the output pollutants, is required [4].

Nowadays, gasoline-fueled Spark-Ignition (SI) engines are the most common propulsive system for passenger cars in the European Union, considering that Hybrid Electric Vehicles (HEV's) also integrate them as their thermal units [5]. Nevertheless, SI engines have considerable disadvantages in terms of efficiency compared to equivalent Compression-Ignition (CI) engines. This is mainly due to the appearance of *knock* in SI engines, an abnormal combustion that compromises their mechanical integrity and prevents the use of high compression ratios [6,7]. Thus, seeing that these powerplants will continue to form part of the automotive market during the following decades, several efforts are being made to integrate solutions in order to mitigate knocking tendencies, seeking an improved engine performance.

One of the most efficient ways to achieve this is by using fuels with a higher Research Octane Number (RON) than gasoline, which extends

* Corresponding author.
E-mail address: rpayri@mot.upv.es (R. Payri).

https://doi.org/10.1016/j.applthermaleng.2023.120754
Received 16 December 2022; Received in revised form 31 March 2023; Accepted 8 May 2023
Available online 12 May 2023

their resistance to knock [8]. Among these, Compressed Natural Gas (CNG) arises as viable choice due to the highly developed infrastructure for its production and distribution. This fuel has less carbon-content than gasoline, which reduces the emission of hazardous pollutants and green-house gases (GHG), specially considering that it can be produced by renewable sources [9]. Additionally, the refinement process of CNG is quite easier, reducing the fuel cost [10]. Another interesting alternative is the substitution of the standard Otto cycle camshaft with a Miller cycle camshaft, which is characterized by closing the intake valve at an earlier stage. This strategy controls the maximum pressure and temperature at full loads, enabling the increase of the engine compression ratio, and also allows to reduce the pumping loses at partial loads, improving the volumetric efficiency of the engine [11,12].

During recent years several investigations have been carried out to evaluate the use of these strategies as potential technical definitions for future SI engine architectures. Aghahasani et al. [13] studied the effects of Natural Gas Direct Injection (NGDI) on the performance and knock behavior of a light-duty SI engine by Computational Fluid Dynamics (CFD), proving that at full load and for a compression ratio of 12.5:1 the knock intensity was extensively reduced as the percentage of natural gas increased, also reducing the CO_2 emissions by 23.5% compared to pure gasoline. Wang et al. [14] studied the effects of Miller cycle in a lean burn natural gas SI engine, showing that for a Late Intake Valve Closing (LIVC) the peak in-cylinder pressure and combustion temperature were reduced, leading to lower NO_x formation and an effective knock mitigation strategy. Moreover, Xing et al. [15] performed similar studies but combining the Miller cycle with a higher compression ratio of 14:1, arriving at a configuration that could improve the fuel consumption by 4.1%. However, these investigations on the use of Miller cycle with CNG have mainly focused on heavy-duty engine applications, whereas for light-duty engines there is still an important research gap.

Interestingly, a convergence point for all of these research works is the fact that these strategies have a negative impact on the combustion process itself. In the case of CNG it is due to the lower laminar flame speeds of this fuel compared to gasoline [16,17], resulting in a longer combustion duration which can increase the heat losses through the cylinder walls [18,19], and limit the synergies of the system with Exhaust Gas Recirculation (EGR) due to the need for advancing the spark timing (ST) in order to obtain the maximum power output. On the other hand, for the Miller cycle the deteriorated combustion is due the compromised in-cylinder flow conditions that stem from closing the intake valve at an earlier stage [20]. Thus, another interesting solution that has not been extensively evaluated in the literature is the integration of an enhanced ignition system to this type of engine configuration.

Among several high-energy igniters, the pre-chamber (PC) ignition system, or Turbulent Jet Ignition (TJI), has gained a lot of attention in recent years [21,22]. This strategy consists of locating the standard spark plug inside a confined volume called "pre-chamber". Several holes are manufactured in the bottom part of this pre-chamber, connecting this region with the main combustion chamber (MC) [23,24]. Thus, after the flame propagates inside th pre-chamber and reaches the holes, hot turbulent jets are ejected into the main chamber to ignite this region, accelerating the burn rates. This enables the use of higher compression ratios as the mixture is burned before reaching the auto-ignition delay times for the appearance of knock, and also allows to burn highly diluted mixtures [25,26], which makes it compatible with the use of EGR [27]. In addition, the passive TJI system has a mechanical simplicity that allows it to easily replace the conventional spark-plug, making it an interesting and affordable solution for passenger car applications.

Thus, given that there has not been extensive research on the combination of all these strategies into a single engine configuration, this paper provides novel contributions to the understanding of the cross-effects of these different technologies (operation with CNG and Miller cycle to enable the use of a higher compression ratio, and use of a passive pre-chamber igniter to improve the combustion process) over a potential technical definition for the next generation of high-efficiency SI engines, in order to improve the performance and reduce the environmental impact of future passenger car vehicles.

Furthermore, the main objective of this research is the detailed study of the aforementioned engine configuration. For this purpose, a non-conventional methodology was developed for performing the analysis at different levels with multiple tools, pushing the investigation forwards in a coherent way. Several investigations from the past years have relied on numerical models to overcome the experimental limitations when analyzing the pre-chamber concept for engine applications [28,29]. Therefore, this research work was carried out using a state-of-the-art 3D-CFD model to study the underlying physical characteristics of the employed technologies (in-cylinder fluid-dynamics, pre-chamber scavenge and turbulence generation, and overall development of the combustion process). For this purpose, a relevant high load/speed operating point of the engine map was simulated and compared with experimental data to validate the CFD model. Thereafter, an experimental campaign was carried out to evaluate the proposed engine configuration in several operating conditions, with and without EGR dilution. Finally, WLTP transient driving cycle simulations were carried out in a 1D vehicle model, to compare the fuel consumption and CO_2 emissions of the new engine definition with a conventional SI engine configuration fueled with gasoline.

2. Tools and methodology

A combination of 1D through 3D numerical simulations and experimental campaigns were carried out to perform the studies of this research. Using the real engine geometry, a 3D-CFD model was developed and validated with experimental results for a baseline engine configuration. To enrich the knowledge on the behavior of the passive pre-chamber ignition system, the model validation was done for both gasoline and CNG, in order to study the characteristics of the combustion process using these two fuels. In this section, the experimental setup and the numerical models are described.

2.1. Experimental facilities

A baseline architecture of a 4-stroke turbocharged single-cylinder SI engine was used to carry out the first experimental tasks. These initial experiments were performed for both gasoline and CNG fuels, in a low displacement (404cc) research engine with a geometric compression ratio of 13.4:1. The engine incorporates a Port Fuel Injection system, a cylinder head with a double-overhead standard camshaft, two valves for the intake and two valves for the exhaust, aiming to improve the scavenging and filling of the cylinder. The passive pre-chamber system was installed in the small housing for the conventional spark plug, to make an easy exchange between the conventional SI concept and the pre-chamber concept. The most relevant characteristics of the baseline engine are shown in Table 1. In a later stage of this research, a more extensive experimental campaign was carried out in a new engine architecture with a higher compression ratio (15.4:1) and using a Miller cycle camshaft. This will be further explained in the upcoming sections.

The engine used in this research was assembled in a fully instrumented test cell following the scheme of Fig. 1. To simulate boost conditions, an external compressor was used. For controlling exhaust back-pressure, a throttle valve located in the exhaust line after exhaust settling was used. A low-pressure EGR system was placed to provide arbitrary levels of cooled EGR. To measure instantaneous pressure inside the cylinder as well as the intake and exhaust ports, a piezo-resistive sensor was used, with a resolution of 0.2 CAD of high sampling frequency signals. An exhaust analyzer HORIBA MEXA 7100 DEGR was used to measure the air-to-fuel ratio as well as EGR rate; a lambda

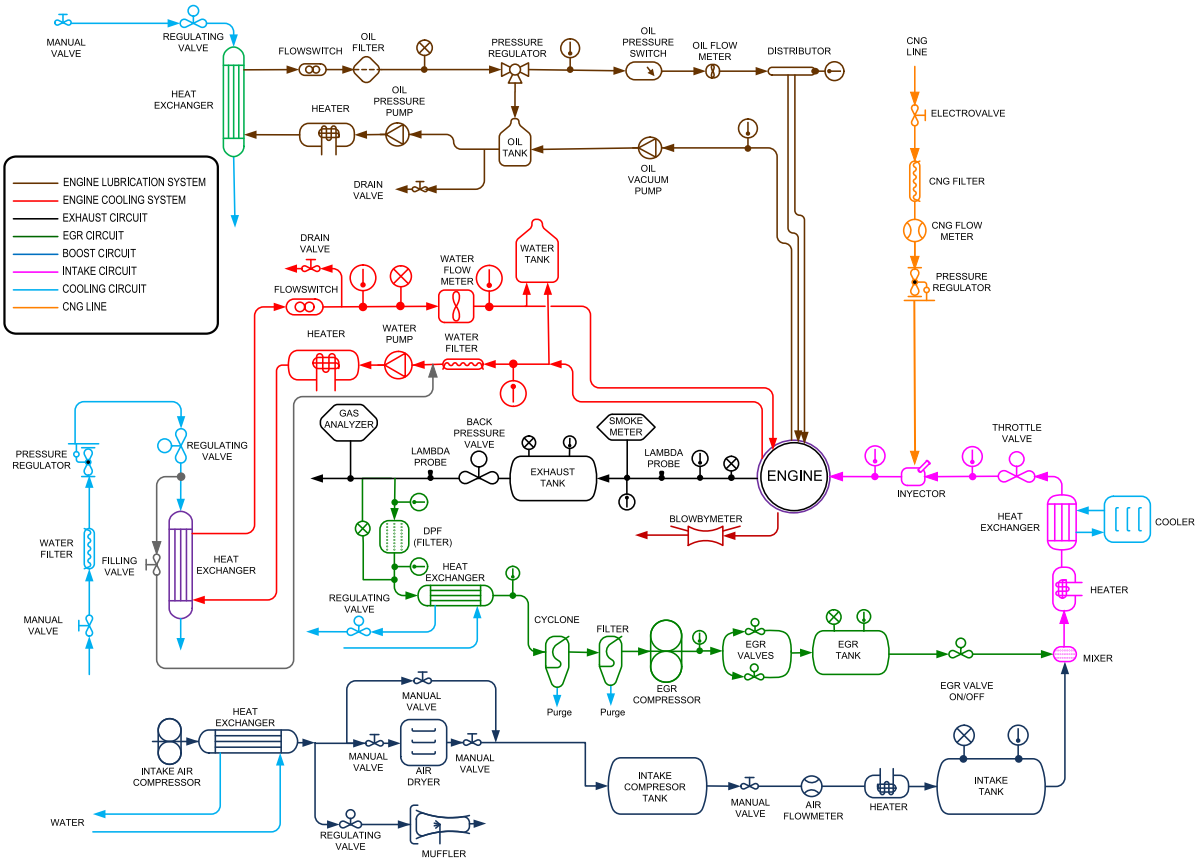

Fig. 1. Test cell scheme.

Table 1
Main specifications of the baseline engine.

Engine	4-stroke SI
Number of cylinders [–]	1
Displacement [cm^3]	404
Bore–Stroke [mm]	80.0–80.5
Compression ratio (geometric) [–]	13.4:1
Valvetrain [–]	DOHC
Number of valves/cylinder [–]	2 intake and 2 exhaust
Fuel injection system [–]	PFI (p_{max} = 6 bar)

Table 2
Test cell equipments.

Variable [Low frequency]	Sensor/equipment	Specification
Engine speed [rpm]	Optical angular encoder	1 to 6000 ± 1
Engine torque [Nm]	Strain-gauges torque-meter	−200 to 200 ± 1
Intake pressure [bar]	Piezoresistive transducer	0 to 10 ± 0.001
Exhaust pressure [bar]	Piezoresistive transducer	0 to 10 ± 0.001
Intake temperature [°C]	Thermocouple K-type	0 to 1000 ± 0.5
Exhaust temperature [°C]	Thermocouple K-type	0 to 1000 ± 0.5
Fluid temperature [°C]	Pt100 thermoresistance	−200 to 850 ± 0.3
Air flow [m^3/h]	Rotary flow meter	0.05 to 160 ± 0.12%
Fuel flow [kg/h]	Fuel Meter AVL 733S	0.05 to 160 ± 0.12%
Blow-by flow [m^3/h]	Flow Meter AVL 442	0 to 4.5 ± 1.5%
Equivalence ratio [–]	UEGO NGK Sensor	0.01 to 2 ± 0.01%
Pollutant emissions	HORIBA MEXA 7100	See Table 3
Smoke level [FSN]	AVL Smoke Meter	0 to 10 ± 2%
Signal [High frequency]	**Sensor/equipment**	**Specification**
Cylinder pressure [bar]	Piezoelectric sensor	0 to 250 ± 0.25
Intake pressure [bar]	Piezoresistive sensor	0 to 10 ± 1%FSO
Exhaust pressure [bar]	Piezoresistive sensor	0 to 10 ± 0.3%FSO
Injection pulse [A]	Clamp-on ammeter	0 to 20 (37 mV/A/10 V)
Injection pressure [bar]	Piezoresistive sensor	0 to 2000 ± 1.5%FSO
Angular speed [–]	Optical angular encoder	1800 pulse/rev (0.2 CAD)

sensor placed at the exhaust pipe was used too for measuring the air-to-fuel ratio. An AVL 577 conditioner was used to control and monitor oil and water temperatures and pressures. To measure the engine fuel consumption, a BRONKHORST F-113AC-M50-AAD-44-V flow-meter was used. Aiming to have complete knowledge of the facilities, the most relevant characteristics of the equipment are described in Tables 2 and 3.

The experimental activities were carried out using a calibrated compressed natural gas (CNG) fuel with a Research Octane Number of 120 (RON120), compared with the reference gasoline fuel with a 95 Research Octane Number (RON95). The main properties of both fuels are described in Table 4. High load and high engine speed conditions (12.8 bar IMEP @4500 rpm) with standard cycle operation were used for comparing the gasoline and CNG fuels, in order to make an initial characterization of the combustion process with the passive pre-chamber ignition concept [30,31].

To calculate cycle-averaged combustion-related parameters, an in-house 0D combustion diagnosis software was used, internally called "CALMEC". Global parameters such as the Indicated Mean Effective Pressure (IMEP), maximum cylinder pressure (P_{max}), pressure gradient ($dP/d\alpha$) and combustion stability indicators (COV IMEP and σIMEP) are derived directly from the analysis of the cylinder pressure signal, while the start of combustion (SoC) and the main burning angles (CA10, CA50, CA90) are obtained from the law of heat release (HR) and the

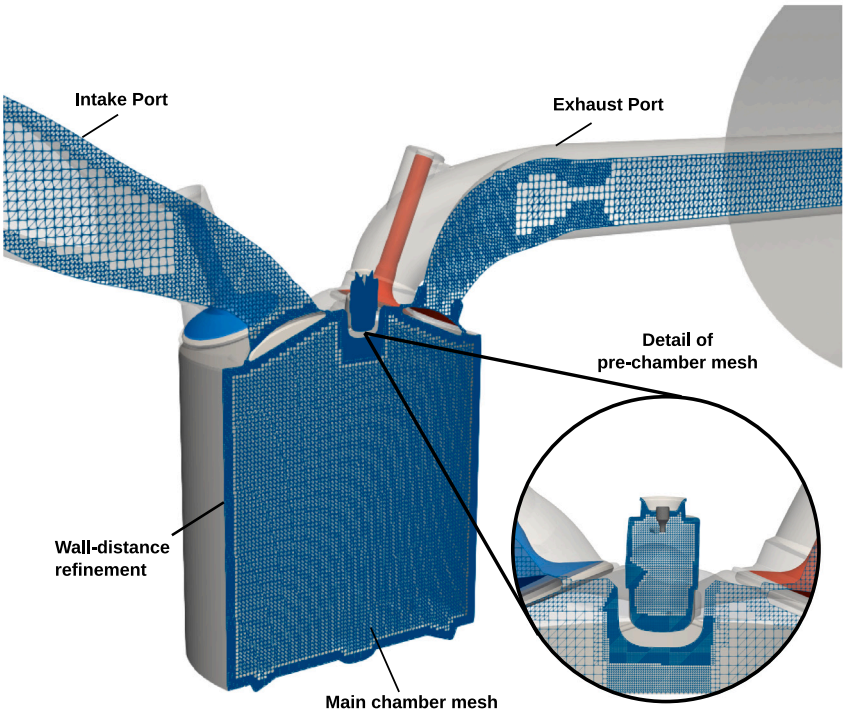

Fig. 2. Computational domain and characteristics of the mesh.

Table 3
HORIBA MEXA 7100 specifications.

Pollutant	Analyzer	Range	Tolerance
HC	FID	min. 0 to 10 ppm C max. 0 to 50 000 ppm C	±4%
NO/NOx	CLD	min. 0 to 10 ppm C max. 0 to 10 000 ppm C	±4%
CO	NDIR	min. 0 to 3000 ppm C max. 0 to 12 vol %	±4%
CO2	NDIR	min. 0 to 5000 ppm C max. 0 to 20 vol %	±4%
O2	PMA	min. 0 to 5 vol % max. 0 to 25 vol %	±4%

Table 4
Main specifications of both fuels.

Type	CNG RON120
H/C ratio [mol/mol]	3.84 mol/mol
O/C ratio [mol/mol]	0.0 mol/mol
A/F_{st} [–]	16.72
Lower Heating Value (LHV) [MJ/kg]	48.931
Density (15 °C) [kg/m^3]	5
Reduced formula ($C_xH_yO_z$)	1.077 (x) – 4.137 (y) – 0.0 (z)
Type	**Gasoline RON95**
H/C ratio [mol/mol]	1.761 mol/mol
O/C ratio [mol/mol]	0.0 mol/mol
A/F_{st} [–]	14.374
Lower Heating Value (LHV) [MJ/kg]	42.793
Density (15 °C) [kg/m^3]	843.8
Reduced formula ($C_xH_yO_z$)	7.594 (x) – 13.376 (y) – 0.0 (z)

heat release rate (HRR), which is estimated from solving the first law of thermodynamics using the measured in-cylinder pressure [32,33].

2.2. Numerical model

To gain further insight on the passive pre-chamber combustion process, a CFD model was developed from the real engine geometry and implemented in CONVERGE [34]. The computational domain is shown in Fig. 2, which includes the intake and exhaust ports and the pre-chamber ignition system.

A brief remark about the pre-chamber alignment with respect cylinder axis is that they are not co-axial, due to the design of the cylinder head. With respect to the employed mesh, hexahedral elements were used, with a base cell size of 4 mm and refinements that go from 0.125 mm for the pre-chamber walls to 0.5 mm for the main chamber walls. The intake and exhaust ports have cells of 2 mm, while inside cylinder the size of the cells is 1 mm. With respect to the pre-chamber region, the cells were refined to a size of 0.25 mm. An Adaptative Mesh Refinement (AMR) algorithm was implemented to improve the grid resolution based on velocity and temperature sub-grid scales of 1 m/s and 2.5 K, respectively, down to a minimum cell size of 0.125 mm. Focusing on the initial flame kernel and the early combustion evolution, the resolution of the mesh was improved up to 0.0625 mm at the spark gap location.

The wall heat transfer model proposed by Torregrosa et al. [35] was used to estimate the initial temperatures for the piston, liner and cylinder head boundaries. the inflow and outflow boundary conditions were taken from the experimental pressure and temperature signals in the intake/exhaust ports. These profiles are shown in Fig. 3 for the baseline engine experiments fueled with both gasoline and CNG at 4500 rpm and 12.8 bar IMEP.

To model the in-cylinder turbulence using an unsteady Reynolds-averaged Navier–Stokes (URANS) framework [36], an eddy-viscosity-based two-equation turbulence model was selected (RNG k-ϵ) [37,38]. This model was chosen due to its accurate predictions of the in-cylinder

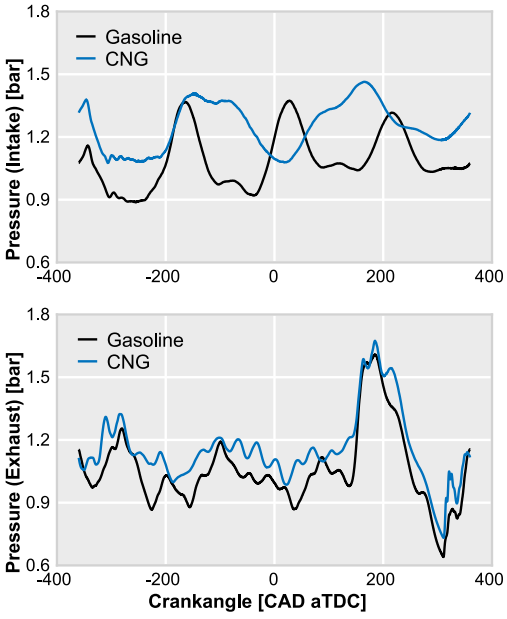

Fig. 3. Experimental intake and exhaust pressures for gasoline and CNG at 4500 rpm and 12.8 bar IMEP.

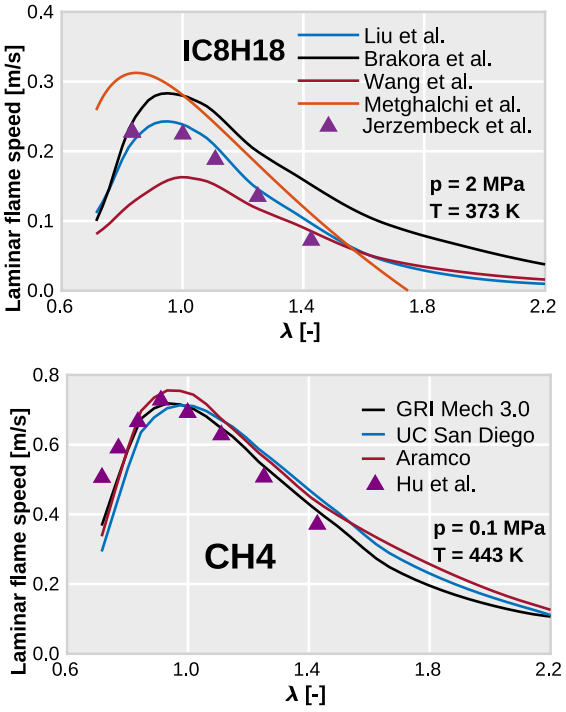

Fig. 4. Laminar flame speed validation for iso-octane and methane.

flow dynamics and improved computational cost compared to other turbulence models [39,40]. The wall functions proposed by Angelberger et al. [41] have been employed to model the heat transfer in the near-wall region, with 3 embedded layers for cells of 0.5 mm added to the cylinder wall boundary. These functions have been calibrated to a set of experiments and account for the quasi-isothermal flow during the compression stroke, and the non-isothermal wall flow during the combustion process. The compressible flow properties were calculated with the Redlich–Kwong equation of state [42].

For combustion modeling, a two-zone flamelet-based model (ECFM) was chosen [43,44]. This model solves a transport equation for the flame surface density (Σ), that allows it to describe the progression of the flame front [45,46]. The main equations solved by the ECFM model are presented below. P_1 in Eq. (2) models the production of flame surface by the effects of turbulent stretch along the flame front. P_2 (Eq. (3)) accounts for the effects of thermal expansion and curvature of the flame. P_3 (Eq. (4)) represents the flame surface production due to mean flow dilation. In this term, $\bar{S}_l$ is the volume-averaged laminar flame speed, while $\tilde{c}$ is the mass progress variable which is calculated by Eq. (6), where $\tilde{Y}_i^b$ represents the burned species mass fraction and $\tilde{Y}_i^u$ represents the mass fraction of un-burned species. Finally, the term D of Eq. (5) is a corrective parameter that accounts for the destruction of flame surface due to consumption. In this equation, β is a model constant defined by the user and $\bar{c}$ is the volume progress variable, calculated in function of the mass progress variable by Eq. (7).

$$\frac{\partial \Sigma}{\partial t} + \frac{\partial u_i \Sigma}{\partial x_i} = \frac{\partial}{\partial x_i}\left(\frac{\mu}{S_c}\frac{\partial(\Sigma/\bar{\rho})}{\partial x_i}\right) + (P_1 + P_2 + P_3)\Sigma - D + P_k \tag{1}$$

$$P_1 = \alpha K_t \tag{2}$$

$$P_2 = \frac{2}{3}\frac{\partial \tilde{u}_i}{\partial x_i} \tag{3}$$

$$P_3 = \frac{2}{3}\bar{S}_l \frac{1-\tilde{c}}{\tilde{c}}\Sigma \tag{4}$$

$$D = \beta \bar{S}_l \frac{\Sigma^2}{1-\bar{c}} \tag{5}$$

$$\tilde{c} = \frac{\sum_i \tilde{Y}_i^b}{\sum_i \tilde{Y}_i^u + \sum_i \tilde{Y}_i^b} \tag{6}$$

$$\bar{c} = \frac{\rho}{\rho_b}\tilde{c} \tag{7}$$

Despite not taking into account detailed chemistry calculations, the ECFM model can describe the turbulent premixed flame propagation very accurately [47]. This leads to a reduced computational time due to a decrease in the use of species transport equations. In addition, the aforementioned model also works with a spark ignition sub-model (ISSIM), that simulates the spark breakdown and discharge by resolving a differential equation for a simplified version of the spark-plug electrical circuit [48,49].

In order to account for the chemical properties of the flame, tabulated values are required by the ECFM model. A Tabulated Kinetic Ignition (TKI) table is needed to consider knocking combustion phenomena, while another table with the laminar flame speeds of the air–fuel mixture is also required. Following the methodology set by Benajes et al. [50,51], the tables were generated by several 0D well-stirred reactor calculations for ignition-delay and 1D laminar flame speed simulations. Thereafter, the tables were arranged for various combinations of temperature, pressure, mixture composition (EGR) and relative air-to-fuel equivalence ratio (λ). A brief example of the aforementioned calculations is presented in Fig. 4, where different reaction mechanisms for Primary Reference Fuels [52–57] were compared with experimental results [58,59]. Pure iso-octane was used as the gasoline fuel surrogate, while pure methane was used as the CNG fuel surrogate. Finally, from the laminar flame speed results shown in the previous figure, the mechanisms from Liu et al. [52] and GRI Mech 3.0 were selected to generate the data tables for gasoline and CNG respectively, as these gave the most accurate predictions of the flame properties.

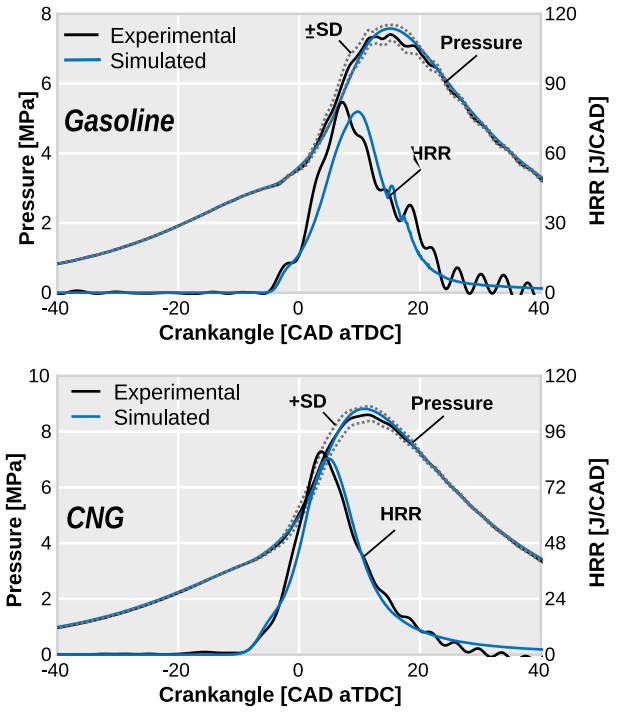

Fig. 5. Model validation for the simulated operating points (high load/speed conditions for both gasoline and CNG).

2.3. Validation of the CFD model

To ensure that the numerical solution is well representative of the real engine physics, a validation of the CFD model is required. Therefore, the experimental results at 4500 rpm and 12.8 bar IMEP were considered for this validation, given that previous investigations performed by the authors have demonstrated the benefits of the passive pre-chamber ignition concept under these high load/speed conditions [30,60]. The experiments correspond to the Maximum Brake Torque (MBT) conditions of each fuel in this running point, using a pre-chamber with the geometrical parameters described in Table 5.

The simulation results are presented in Fig. 5, where the main chamber pressure and HRR traces are shown for both fuels, contrasted against the experimental data averaged over 250 consecutive firing cycles. The fluctuations of the experimental signals have also been included in each plot. As can be seen, for both gasoline and CNG, the CFD model manages to capture the measured pressure profile very accurately, being contained within the experimental error range. The simulated HRR also shows a good behavior in terms of combustion onset, duration and maximum burn rates. However, this parameter is not a strict requirement for the model validation, given that the experimental curve is estimated from a 0D software. In addition, the 3D model was validated against other indicated parameters of the engine, such as the IMEP and the indicated efficiency. As it can be seen in Table 6, the simulations provided accurate predictions with an error below 1%, further verifying the robustness of the numerical solution. These results provide a solid foundation for performing a detailed study of the combustion process with the CFD model.

2.4. Methodology

The studies presented in this research work consist of a combination of experimental activities and numerical simulations. A methodology loop composed by 4 stages was defined for this investigation. In the first stage, the conventional SI and passive pre-chamber concepts are compared in the baseline engine configuration, operating in un-diluted stoichiometric conditions ($\lambda = 1$) with gasoline and CNG fuels. This activity was performed with the aim of investigating the impact of the fuel on the passive pre-chamber combustion process, and the benefits of the concept considering knock limited and non-limited conditions. For this purpose, an operating point combining both high engine load and speed (4500 rpm @12.8 bar IMEP) was selected to make the comparison. The measurement methodology considered in these experiments was the same as previous researches [61,62], optimizing the spark-timing to achieve MBT conditions. It is important to point out that to make an adequate comparison, and considering that the Lower Heating Values (LHV) of both fuels are different, the mass was adjusted in each case to release the same amount of energy (iso-IMEP conditions).

The second stage of this research focused on the transition to a new engine architecture, integrating technological bricks to further exploit the advantages of using CNG and the pre-chamber system. This engine configuration includes the addition of a Miller cycle camshaft and the increase of the geometric compression ratio. Furthermore, the CFD model was used to pre-evaluate this new engine architecture in terms of main chamber and pre-chamber scavenge, turbulence generation and combustion process.

In the third stage, the new engine definition was set up on the test bench, in order to carry out a broad experimental campaign at different speeds and loads, aiming to generate full engine maps for stoichiometric conditions, both with and without EGR. The experimental conditions for this activity are described in Table 7, that consist of 3 valid repetitions for each running point, in order to obtain a trusted average value. Finally, in the last stage of the research real driving cycle simulations were carried out to assess the performance of the new engine. A 1D model was implemented in GT-Power to simulate the full vehicle, operating with a conventional SI engine architecture using gasoline and the new engine definition using CNG and the passive pre-chamber concept. The results for both powerplants are compared in terms of fuel consumption and CO_2 emissions during the driving cycle.

Table 5
Main specifications of the pre-chamber.

Geometric parameter	Value
Volume [mm^3]	600
Number of holes	6
Holes diameter [mm]	0.7
A/V ratio [1/m]	3.9

Table 6
Comparison of indicated parameters for the baseline engine simulations and experiments at 4500 rpm and 12.8 bar IMEP.

Employed fuel	IMEP [bar]		Indicated eff. [%]	
	Experimental	Simulated	Experimental	Simulated
Gasoline	12.8	12.85	43.4	43.5
CNG	12.8	12.93	41.8	41.9

3. Results and discussion

This section presents and analyzes the experimental and numerical results of the research, focused on the optimization of the engine architecture to operate with CNG and the passive pre-chamber concept. For this purpose, the experimental results will be compared against the CFD model with 2 configurations equipped with the passive pre-chamber ignition system. First, the baseline engine, with the specifications that were shown in Table 1, and then for the second configuration, the engine with Miller cycle and increased compression ratio.

Table 7
Operating conditions for mapping the new engine architecture.

	IMEP [bar]	Engine speed [rpm]
Point 1	3.50	1250
Point 2	10.0	1250
Point 3	8.50	1750
Point 4	12.0	1750
Point 5	3.50	2000
Point 6	8.50	2000
Point 7	13.6	2000
Point 8	6.00	2500
Point 9	12.0	2500
Point 10	3.50	3000
Point 11	8.50	3500
Point 12	3.50	4000
Point 13	13.3	4000
Point 14	14.0	4000
Point 15	11.0	1250
Point 16	14.0	1250
Point 17	11.4	1500
Point 18	12.5	1500
Point 19	15.0	1500
Point 20	15.0	1750
Point 21	15.0	2000

3.1. Analysis of the baseline engine architecture

This first study with the base engine configuration has been carried out under stoichiometric conditions and without using EGR, at high load (12.8 bar IMEP) and high speed (4500 rpm) [30]. The most relevant results of the experimental hood are summarized in Fig. 6, where 3 important parameters related to the combustion process are shown in bar graphs, the CA50 (combustion phasing) which indicates the crankangle at which 50% of the fuel mass has been burned, the σIMEP which represents the cyclic variability of the mean effective pressure, and the indicated engine efficiency. Regarding to the black bar, it represents the results using the conventional spark plug while the blue bar shows the results using the passive pre-chamber. The dashed horizontal lines highlight the values of each particular parameter with the conventional spark plug.

When operating with gasoline, the indicated performance of the engine increases from 40.3% to 43.4%, or by 3 percentual points, when switching from the conventional spark plug to the pre-chamber, which translates into an efficiency improvement of 7.7%. This increase in efficiency is due to the appearance of the knocking phenomenon when operating in these conditions with the conventional SI concept, due to the combination of high pressure and temperature reached by the high compression ratio of the engine. This prevents CA50 values closer to TDC from being reached, since very small variations in the ignition timing cause a significant increase in the cycles where knocking appears, generating inadmissible values of σIMEP (over 10%). However, when using the pre-chamber, the increase in heat release rate allows to mitigate the knocking trend, obtaining CA50 values closer to TDC and improving combustion stability, which leads to an increase in thermal efficiency.

On the other hand, when operating under the same conditions but using CNG as fuel, this behavior is no longer observed. The engine performance using the spark plug and the pre-chamber are the same. This is mainly due to the fact that with CNG the knocking phenomenon no longer appears, since the fuel has a higher octane number (RON120). For this reason, the advantages of the accelerated combustion of the pre-chamber are no longer reflected in the performance of the engine, given that with both ignition systems an optimum CA50 can be achieved. However, from this experimental campaign it is not possible to obtain more details on how the combustion process evolves inside the main chamber. For this reason, the developed CFD model was used

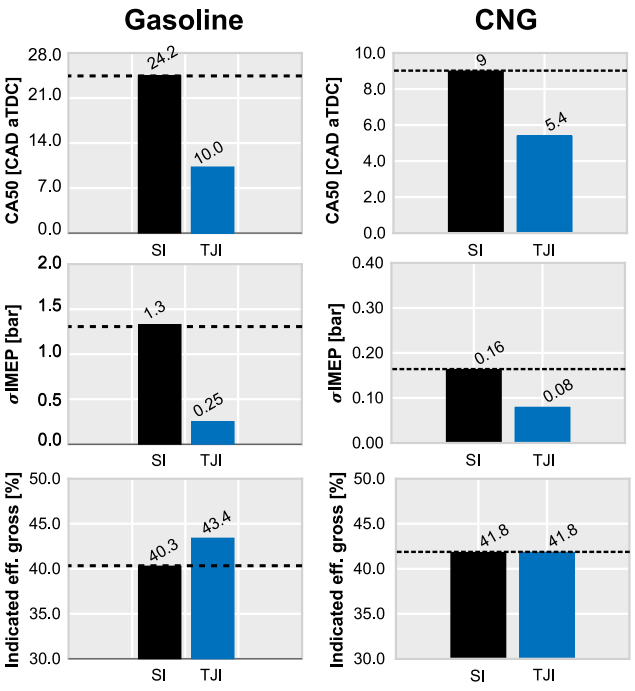

Fig. 6. Experimental results for the baseline engine at high load/speed conditions (12.8 bar IMEP @4500 rpm) fueled with gasoline and CNG at $\lambda = 1$ without EGR.

to further study these results, and try to understand the underlying thermochemical and physical characteristics that can help to optimize the engine design for CNG use.

To better understand the combustion process with the pre-chamber, Fig. 7 shows a series of snapshots at different crankangle degrees after the Spark timing of each case (CAD aST), to observe the evolution of the flame propagation in the main chamber for both gasoline and CNG. Highlighted in green are the limits of the jets, which are calculated with a user-defined function programmed into the CFD code for this research work, and in the color scale the source term of the energy equation is shown, which represents the flame itself. On the other hand, the right-side of the figure presents two graphs, where the heat releases are shown for each case, divided into the amount of energy consumed inside the jets (blue curve), the energy released outside the jets (black curve) and the total HRR (red curve). As it can be seen, the combustion pattern is very similar for both fuels, where the flame starts to develop inside the jet boundaries and then is able to progress outside these boundaries and propagate as a conventional SI engine flame front. It is noteworthy that the mixture burns mostly outside of the jets. For the case of gasoline, approximately only 25% of the mixture is consumed inside the jets, while for CNG, it increases slightly although it does not exceed 35% of the total mass of the main chamber.

Regarding the combustion process inside the pre-chamber, Fig. 8 shows 4 graphs: in the top one, the laminar flame speed is observed; in the middle graphs, the pressure differential (Δp) between the pre-chamber and the main chamber and the momentum of the jets are plotted; and finally, the bottom plot shows the main chamber pressure for both fuels. All of them present on the horizontal axis the evolution of the crankangle referenced to the spark timing (CAD aST). It can be observed how the laminar flame speed of CNG is lower than for gasoline, which slows down the combustion process for this fuel. Consequently, the reduced burn rates have a direct impact over the jet ejection parameters. As the combustion is slower inside the pre-chamber, it is observed that the peak pressure differential generated for CNG is around 30% lower, as well as the maximum momentum flux of the ejected jets. However, the ejection parameters are also affected

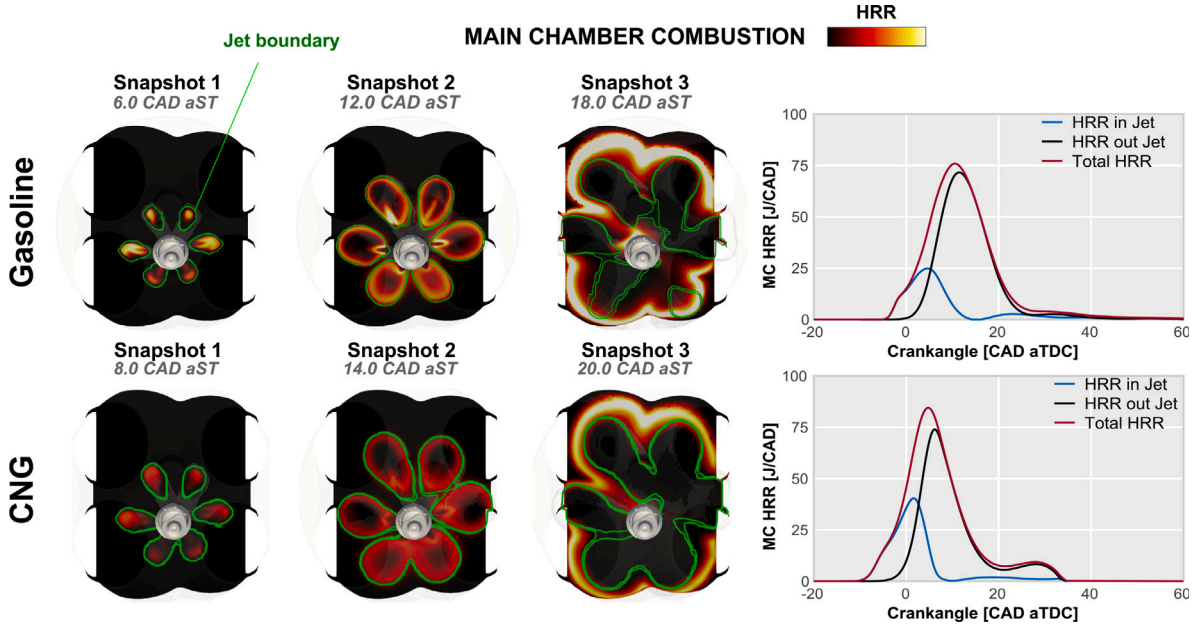

Fig. 7. Visualization of the main chamber combustion process using gasoline and CNG. The heat release in the main chamber is presented on the right side, divided into the amount of mass consumed inside and outside of the jets.

by the higher main chamber pressure that they need to overcome, as it can be seen in the bottom plot. Given that the stoichiometric air-to-fuel equivalence ratio of CNG is higher than gasoline, greater intake pressures are needed to reach this value (see Fig. 3 for reference), thus increasing the cylinder pressure at the Intake Valve Closing (IVC).

Additionally, another interesting study of the combustion process with the pre-chamber can come from analyzing the flame surface that is generated, since in essence, the TJI system consists of a large and distributed surface ignition instead of a localized spot ignition like that of a conventional spark plug. In Fig. 9, the flame surface evolution for CNG and gasoline is presented. This figure also shows a three-dimensional representation of the flame for an SI engine with a conventional spark plug and an SI engine equipped with the passive pre-chamber concept, at 15 CAD after their respective spark timings. From this plot, it can be observed that the TJI concept generates a flame surface which is over 4 times greater than the conventional spark plug. Additionally, it is seen that when operating with CNG the generated surface is higher than for gasoline. This is mainly due to the different in-cylinder flow conditions discussed in the previous figure.

Having a larger flame surface helps to consume more fuel mass per square meter, as long as competitive levels of combustion velocities (laminar + turbulent) are maintained. Furthermore, with the analysis presented, it makes sense to use the combination of CNG with the pre-chamber concept, as the reduced laminar flame speeds can be overcome by the higher turbulent flame speeds generated with the TJI combustion system, and having a larger flame surface than gasoline also presents a considerable advantage when combining these two technologies. However, other modifications to the engine architecture must be made to take advantage of the intrinsic properties of natural gas and improve combustion in the pre-chamber to obtain better jets.

3.2. Transition to the new engine architecture

In view of the results obtained with the base configuration, it is necessary to implement improvements in the engine if the advantages offered by the use of CNG and the TJI system are to be fully harnessed. As anticipated in previous sections, one of the main changes in the new configuration is the increase of the geometric compression ratio from 13.4:1 in the base engine to 15.4:1. This value was selected to operate the new engine architecture in equivalent (similar) conditions at TDC compared to the original engine architecture in terms of knock limitations of both fuels (gasoline for the original engine configuration and CNG for the new engine configuration). This way, the potential benefits of the accelerated combustion generated with the pre-chamber system can be truly exploited.

On the other hand, the second important modification with respect to the base configuration is the use of the Miller cycle. The main purpose of this change in the cycle is to increase engine efficiency and reduce pumping losses [12]. It should be remembered that the use of a Miller cycle can impair both turbulence generation and the sweep of residual gases that remain in the cylinder due to the early closure of the intake valve. However, this can be compensated for with the use of a higher compression ratio and the passive pre-chamber. Compared to a standard Otto cycle in a conventional SI engine, looking at Fig. 10, the valve lift profiles are slightly different. In this figure, the solid lines correspond to the intake valve profiles, while the dashed lines correspond to the exhaust valves. The main difference lies in the advance of the Intake Valve Closing when using a Miller cycle, which significantly reduces the pumping work of the engine.

The next step in the investigation was to use the previously calibrated CFD model for CNG to simulate the new engine configuration under the same operating conditions as previously described (high engine load/speed), and using the same fuel (CNG). These results were compared with those of the baseline engine, both operating with the passive pre-chamber system. Fig. 11 shows the filling of the cylinder and the pre-chamber with fresh gases coming from the intake. It can be seen that the use of a Miller cycle leads to a slight decrease in the amount of fresh mixture entering the cylinder, about 4% less. This trend is also present in the pre-chamber; however, as the cycle approaches TDC, the final amount of fresh mixture in this region hardly differs by 1%. This is mainly due to the increase in compression ratio, as the pre-chamber is effectively filled during the compression stroke [50,63]. For

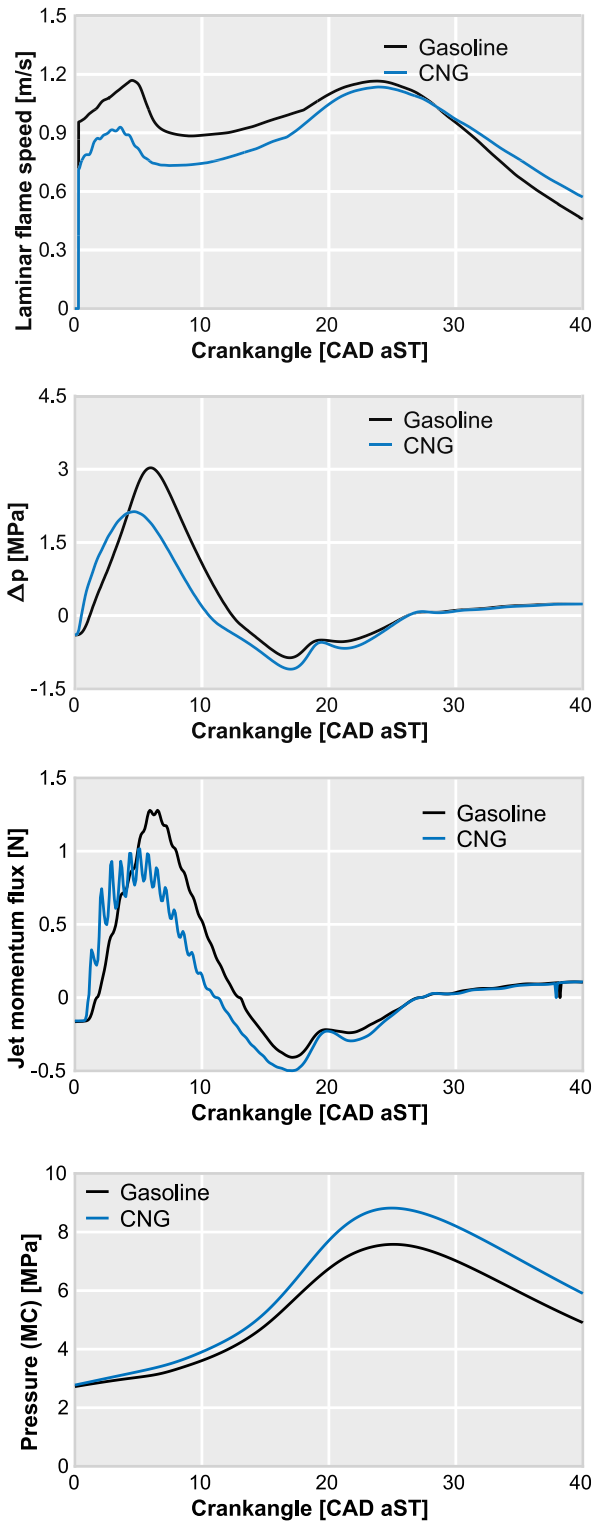

Fig. 8. Laminar flame speeds, jet ejection parameters (Δp and momentum flux) and in-cylinder pressure for the baseline engine configuration fueled with gasoline and CNG.

this reason it does not present as large a difference as the main chamber in terms of un-scavenged residual gases.

In addition to compromising the amount of un-swept residual gases, the use of the Miller cycle also influences the generation of turbulence in the cylinder. Looking at the top graph in Fig. 12, a large difference in the turbulent kinetic energy (TKE) levels in the main chamber during the intake stroke can be observed. Although these levels then balance out during compression, the middle graph shows a 20% reduction in TKE levels at spark timing (15 CAD before TDC). However, due to the increased compression ratio, the trend inside the pre-chamber is reversed. Due to the higher pressure differential between the main chamber and the pre-chamber, the gas exchange process generates 25% higher TKE levels at the moment of ignition in the new configuration using the Miller cycle.

As a direct consequence of the higher levels of turbulence, the combustion process inside the pre-chamber is accelerated. This fact can be appreciated in Fig. 13, where both the HRR profile and pressure in the main chamber are plotted for the standard and Miller cycle configurations. Here, an earlier combustion onset is observed for the new engine definition, which in combination with the higher pressure generated during the compression stroke due to the increased compression ratio, lead to a higher pressure profile during the combustion process.

Finally, in spite of the degradation of turbulence inside the cylinder and the increase of un-scavenger residual gases, this new engine configuration is able to achieve a faster combustion inside the pre-chamber, leading to better jets ejected towards the main combustion chamber. Therefore, this leads to an increase of the indicated engine efficiency of around 3% with respect to the baseline engine architecture operating with CNG.

3.3. Experimental characterization of the new engine architecture

After highlighting the expected benefits of the new engine architecture, this section focuses on characterizing the behavior of this new engine configuration fueled with CNG in the engine map, discussing the impact of using a high-octane fuel and an advanced ignition strategy. Likewise, the impact of implementing EGR in terms of consumption, combustion stability, knocking and heat release is also discussed.

The most relevant combustion-related parameters for stoichiometric conditions without EGR are presented in Fig. 14, where the results for the 21 points described in Table 7 are shown. In this figure, the top-right plot shows the Maximum Amplitude Pressure Oscillation (MAPO), a method of knock detection that relies on the frequency domain processing of the in-cylinder pressure signal data, which is studied in detail by Siano et al. [64]. Taking into consideration that 3% to 5% of heavy knock events are judged to be acceptable for the engine operation, this criterion was applied to define the admissible MAPO values. In the top-left plot, from mid to high engine speeds and loads, high indicated efficiency levels are observed, particularly at high speed/load conditions where a 44.2% efficiency is achieved. This matches the 3% efficiency gain that was expected from the CFD results of Fig. 13, recalling that for the baseline engine definition the efficiency levels in these conditions were below 42% (Fig. 6). On the other hand, the efficiency levels drop considerably when operating at low engine speeds.

Particularly, at low speed and high loads (low-end torque map region), significant issues are shown that compromise the operation of the engine, as can be seen in the bottom-left and top-right plots. The advanced CA50 values indicate that combustion in this region of the map cannot be shifted towards the expansion stroke due to combustion stability problems. As a result of the advanced combustion phasing, loads in the low-end torque map region are limited by knock (high MAPO values) and MBT conditions cannot be reached, leading to a very negative impact on the levels of efficiency. In addition, as it can be seen in the bottom-right plot of Fig. 14, in the low-end torque map region the combustion duration is considerably reduced.

This last remark is better observed in Fig. 15, where the main chamber HRR is plotted for both the conventional SI concept and the passive pre-chamber concept in the highlighted conditions of the engine map. The HRR profiles of points 1 and 3 show a similar combustion

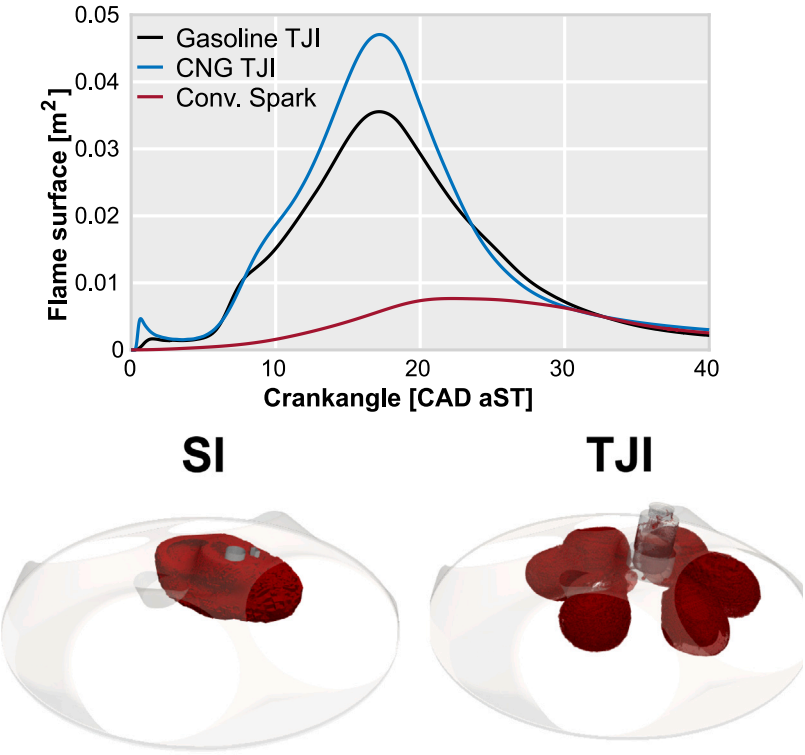

Fig. 9. Flame surface for gasoline and CNG combustion in the baseline engine using the passive pre-chamber system. The flame surface generated in a gasoline-fueled SI engine using the conventional spark plug is also shown for reference. The 3D snapshots are taken for a crankangle of 15 CAD after the respective spark timings.

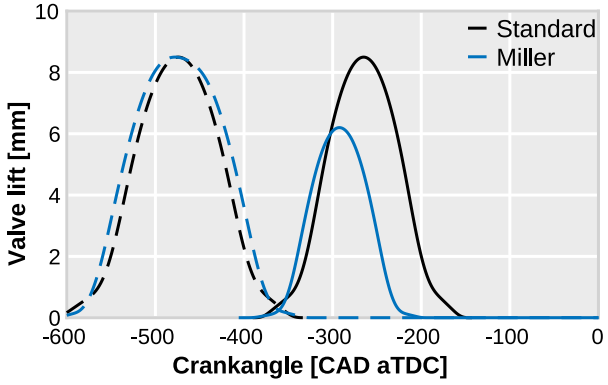

Fig. 10. Valve lift profiles for standard and Miller cycles.

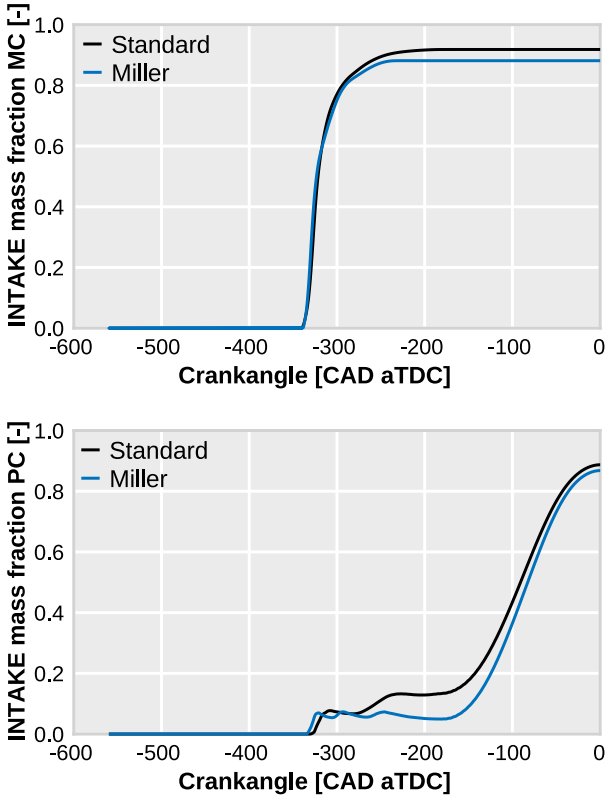

Fig. 11. Mass fraction of fresh gases in the pre-chamber and main chamber for the standard and Miller cycles operating with CNG.

phasing between both ignition systems, which leads to a suitable performance in those conditions. However, for point 2 (low-end torque), the combustion process for the pre-chamber is considerably faster, advancing the CA50 even earlier than the TDC. In this point, trying to delay the spark timing results in inadmissible levels of cycle-to-cycle variability (CCV), which prevents the achievement of higher engine loads. Furthermore, it can be observed that the advanced combustion phasings caused by the accelerated burn rates of the TJI system can lead to a knocking trend, as was observed in the MAPO values of Fig. 14.

On the other hand, the same conditions were tested but with the addition of EGR. The EGR levels were controlled by regulating the output pressure of the EGR compressor, as well as by regulating the EGR valves through the PID controllers in order to achieve a finer tuning. The dilution levels (EGR), which are shown in the top-left plot of Fig. 16, were targeted to maximize the gross indicated efficiency at

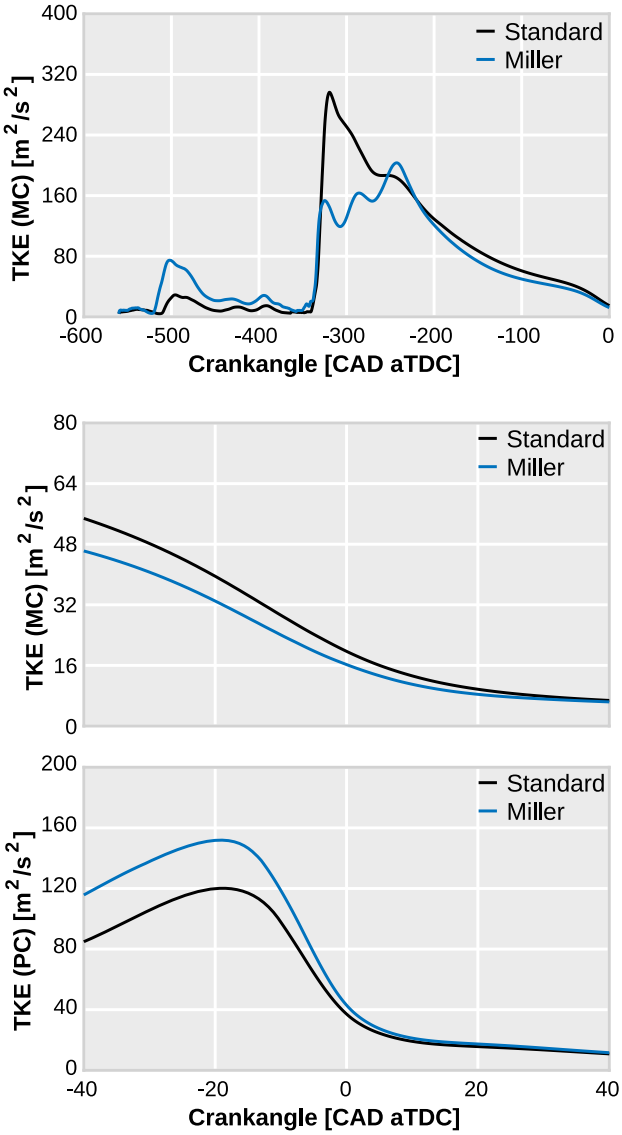

Fig. 12. Comparison of turbulent kinetic energy in the pre-chamber and main chamber for Standard and Miller cycles operating with CNG, (Top) Intake stroke, (Central & Bottom) Compression stroke.

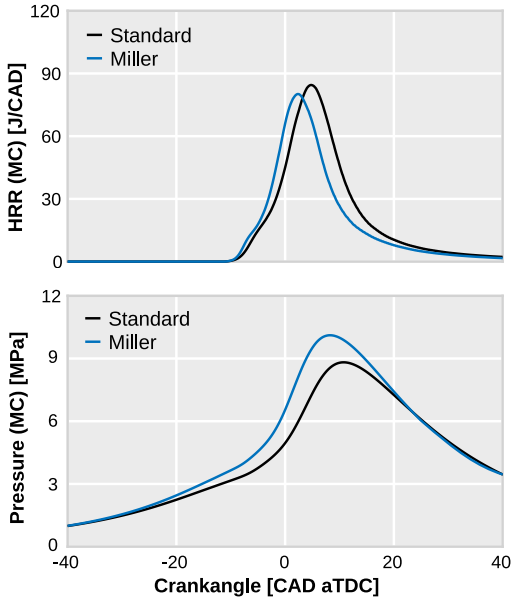

Fig. 13. HRR and pressure in the main chamber for Standard and Miller cycles operating with CNG.

each operating point. According to the top-right and bottom-right plots, the first remarkable aspect that can be observed is the significantly longer combustion duration at low loads in the entire engine speed range. Thus, the CA50 values are shifted towards the expansion stroke at the same time as the EGR rate is increased, even operating at high loads and low speeds, which allows to achieve optimum combustion phasings in all the tested conditions. According to this, the addition of EGR allows to extend the load limit as it increases the combustion duration, eliminating the aforementioned issues related to the extremely fast burn rates achieved with the pre-chamber in the low-end torque region of the map. Additionally, the efficiency levels in the whole engine map are improved by adding EGR.

Going further in detail with the experimental results of the test campaign, the impact of EGR was analyzed in terms of knocking and combustion stability parameters in Fig. 17. This figure shows, in the top-left and top-right plots, the Maximum Amplitude Pressure Oscillation (MAPO) and covariance of the IMEP (COV IMEP) respectively for the tests without EGR, and the same distribution in the row below for the EGR tests. As it can be observed, the knock trendy area of the tests without EGR (high MAPO values at the low-end torque region) is also translated to increases in the cyclic variability of combustion (COV IMEP). This is a product of the accelerated combustion rates achieved with the pre-chamber in these conditions (shown in Fig. 15), which prevents the engine from achieving suitable CA50 values. The limit of acceptable cyclic variability according to the literature and considered for this investigation is between 3% and 5% of the IMEP (depending on the operating conditions).

Nevertheless, the previous low stability zone is avoided when the EGR strategy is applied. This means that a new available operating range at low/mid speed and high load is obtained when the EGR is used. on the other hand, EGR has a negative impact on combustion stability at low engine loads and high engine speeds as shown by the bottom-right plot of Fig. 17, which can be explained due to the shorter time to scavenge the pre-chamber plus the lower in-cylinder temperatures reached during the combustion process.

In order to finish the experimental results, the fuel consumption was analyzed in Fig. 18 to complete the understanding of this new engine architecture. The same plot distribution as the previous figure was used, in which the upper part shows tests without EGR and the lower part tests with EGR. Likewise, the left part shows the gross consumption and the right one corresponds to the net consumption. The first fact that can be observed is the reduction in fuel consumption with the addition of EGR due to a better combustion phasing. As expected, pumping losses are reduced when operating with EGR, specifically at low engine speeds. Another fact that can be observed, is the correlation of combustion stability with the fuel consumption operating with EGR at high engine speeds and low load.

3.4. Driving-cycle simulations of the new engine architecture

For the final part of this research, driving-cycle simulations were performed in order to analyze a real application viability for the new engine architecture. The simulations are based on a transitory driving-cycle WLTP (World Harmonized Light-duty vehicle test Procedure). This is a global standard procedure in which the main goal is to determine pollutants, CO_2 emissions and fuel consumption in conventional light-duty vehicles, hybrids and pure electric vehicles. This test

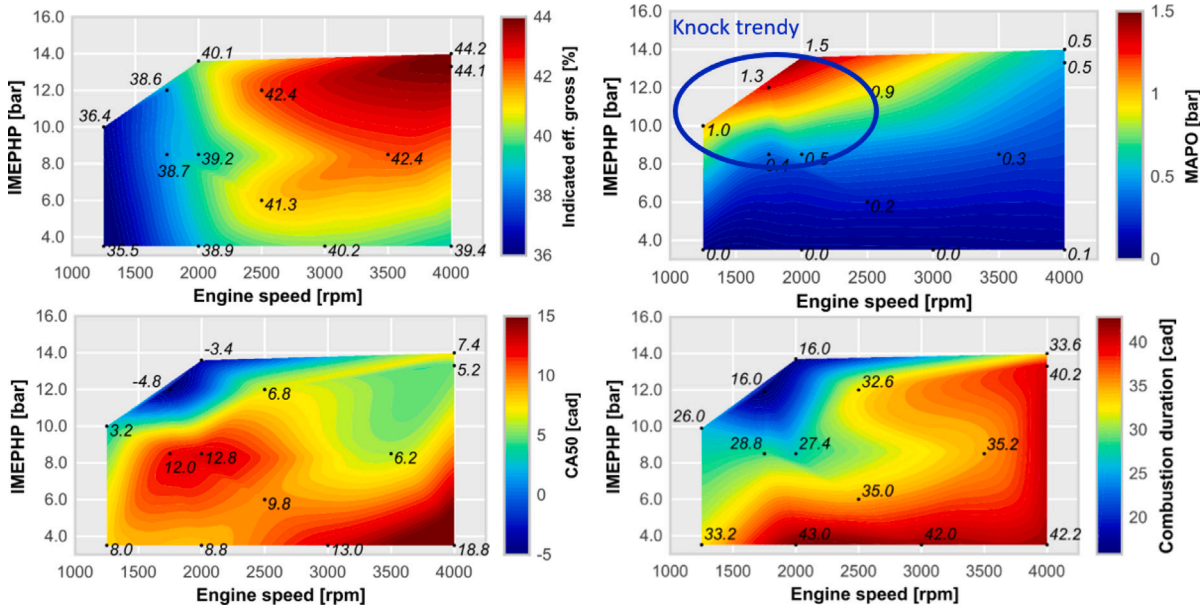

Fig. 14. Maps of the new engine architecture fueled with CNG without EGR.

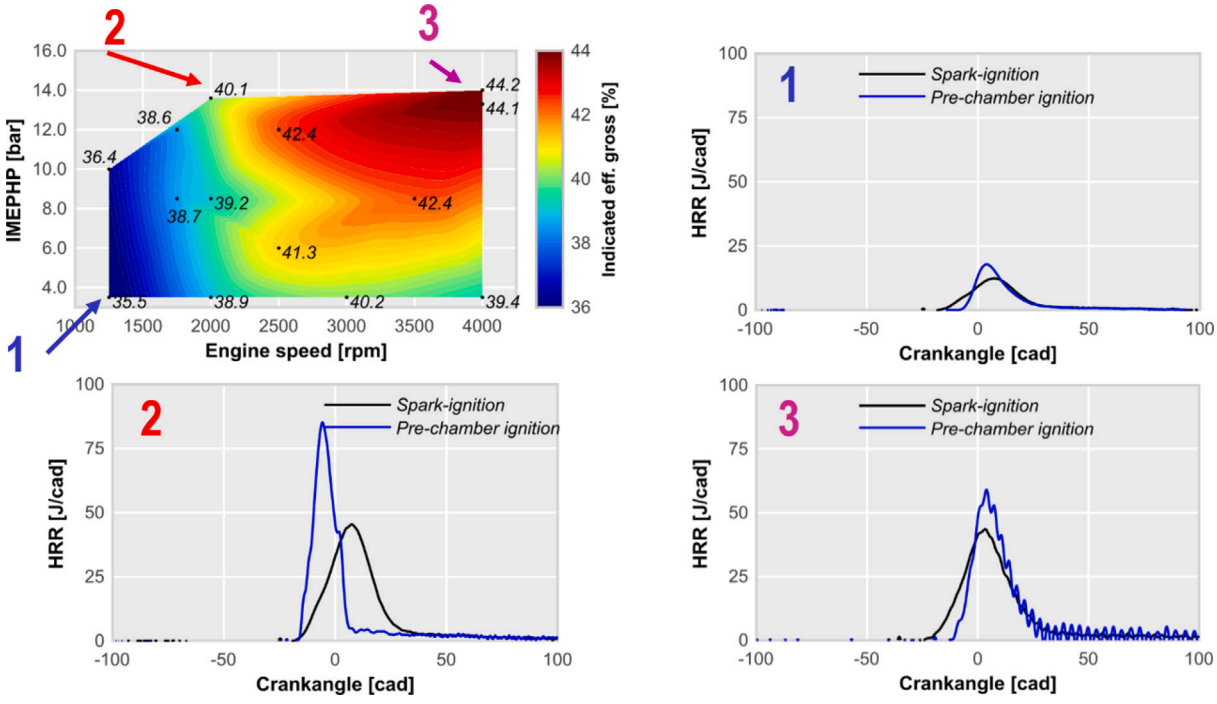

Fig. 15. Analysis of 3 edges of the engine map: high load/speed conditions (point 3) low load/speed conditions (point 1) and low-end torque (point 2).

procedure was developed by the United Nations Economic Commission for Europe (UNECE).

Furthermore, this procedure was applied to a 1D dynamic model in GT-Power. A class 3 standard vehicle was simulated, equipped with a 4-cylinder engine, based on the previously investigated single-cylinder engine, with a total displacement of 1.6 liters. The model has been configured for benchmarking the performance of a standard SI engine fueled with RON95 gasoline with those generated by the new engine definition (Miller cycle, higher compression ratio and TJI system) operating with CNG fuel.

Two different vehicles were simulated in order to compare the previously mentioned engine definitions. The first one, is a conventional vehicle with a standard SI engine, operating with a compression ratio of 10.5:1, without Miller cycle and keeping lambda 1 in the whole engine map (without over-fueling). The second one, swaps the engine to one fueled with CNG, setting the compression ratio to 15.4:1, equipped

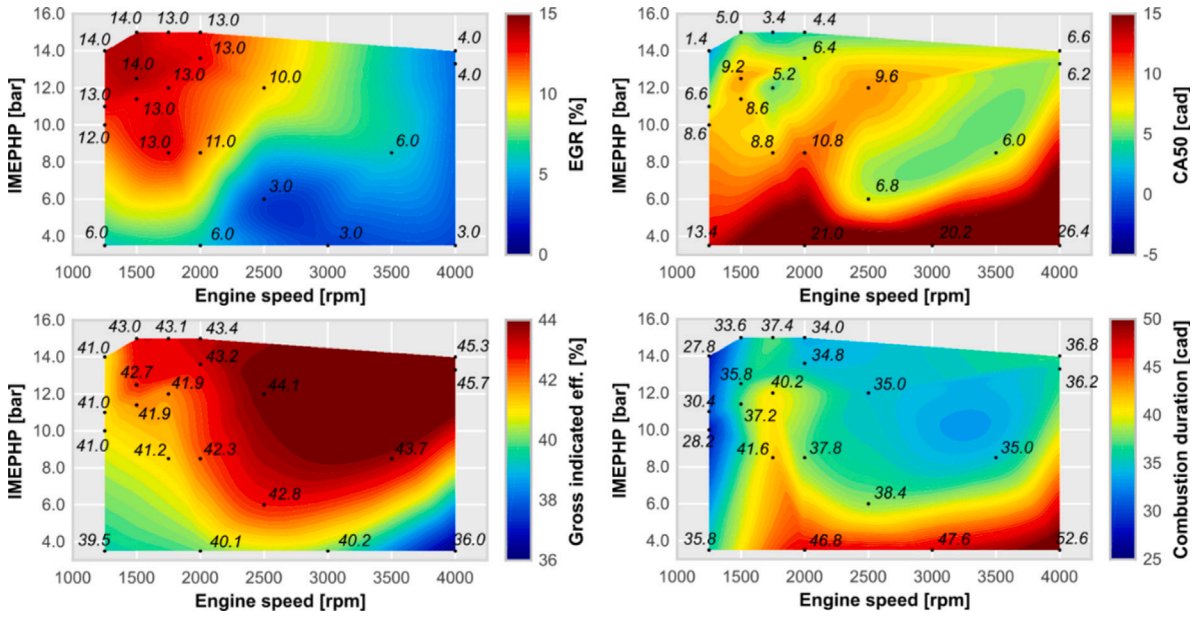

Fig. 16. Maps of the new engine architecture with EGR and CNG fueled.

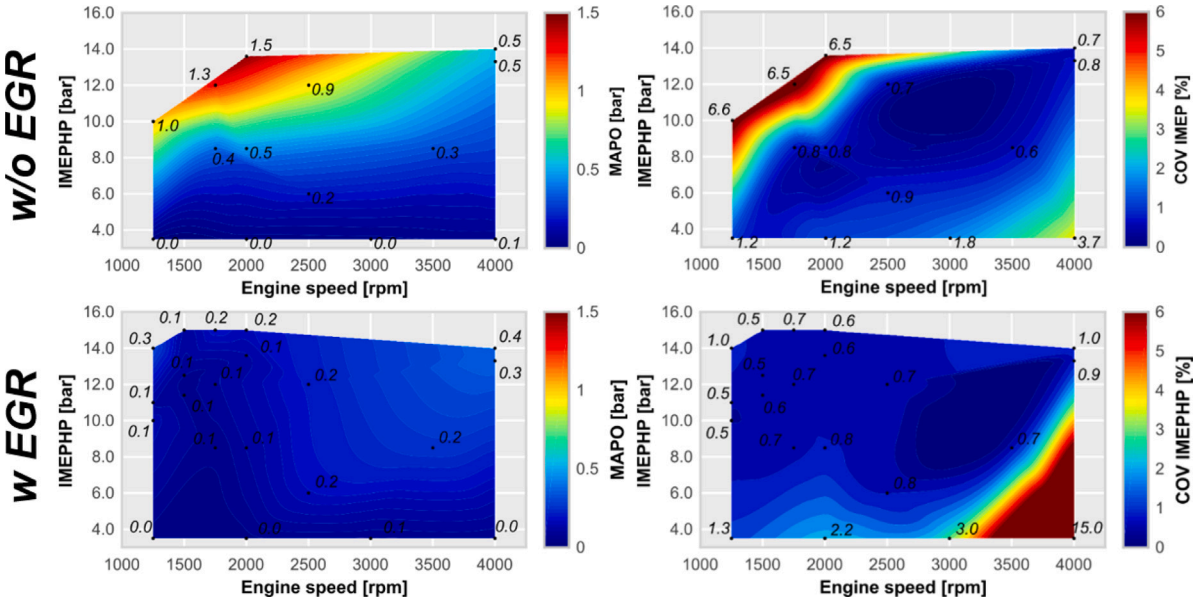

Fig. 17. Comparison of the new engine architecture with and without EGR: combustion stability and knocking trend.

with a passive pre-chamber system and operating with a Miller cycle camshaft, unless the intake pressure demands during accelerations forces to switch to the standard camshaft, in order to follow the dynamics of the driving cycle, somehow imitating a Variable Valve Timing (VVT) system.

The following experimental input data was used for the model configuration:

- Basic geometrical data: Cylinder bore, stroke, connecting rod length.
- Valve timings and profiles for the selected camshafts.
- Combustion process profiles: Heat Release Rates (Wiebe functions) calibrated to the database generated from the experimental cylinder pressure analysis (following the standard methodology, the model interpolates the Wiebe function parameters in those operating conditions not directly evaluated experimentally). These profiles use pre-tabulated values for the start of combustion (CA10) and the combustion duration (CA10-90), which change depending on the engine load and speed, as well as including corrections for transient conditions. The combustion profiles in each engine were calibrated for their respective operating points.
- EGR rates: They were kept equal for both engine architectures as the tolerance of the new engine configuration to EGR was proven to be similar than that of a standard SI engine.

In view of the results that can be seen in Fig. 19, the enormous potential of the new engine definition can be seen. With regard to the first graph, it can be seen how the total fuel energy required to perform the WLTP driving cycle has decreased by approximately 5% compared to the conventional SI engine. Furthermore, considering fuel consumption (central graph), this difference increases to approximately 15%, a more than remarkable and expected decrease in consumption, taking into account the high calorific value of CNG compared to commercial RON95 gasoline. Finally, it should be remembered that the

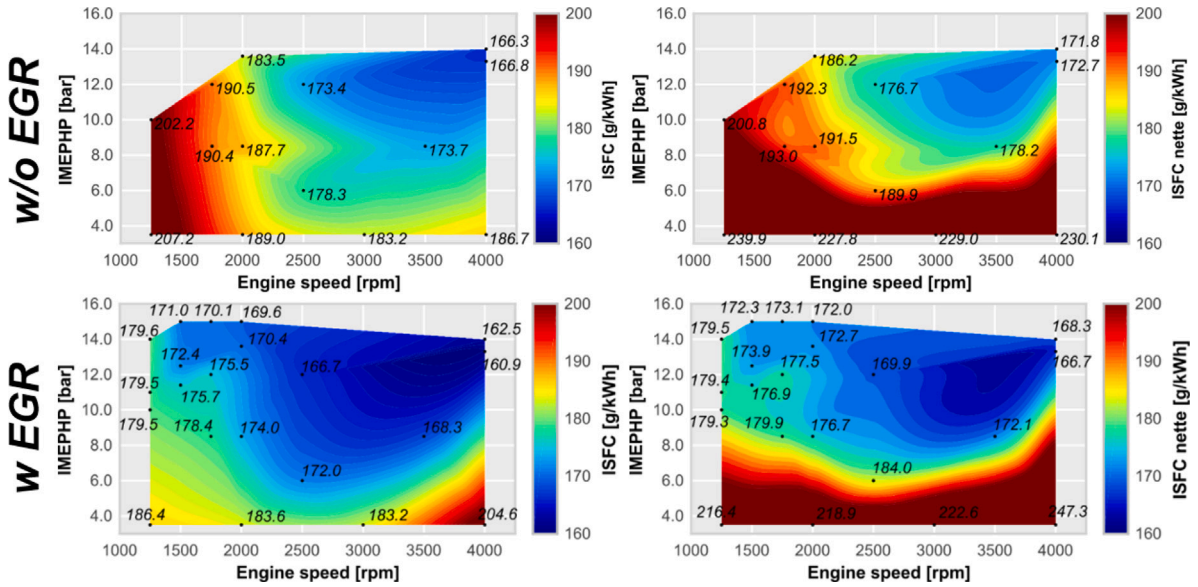

Fig. 18. Comparison of the new engine architecture with and without EGR: fuel consumption.

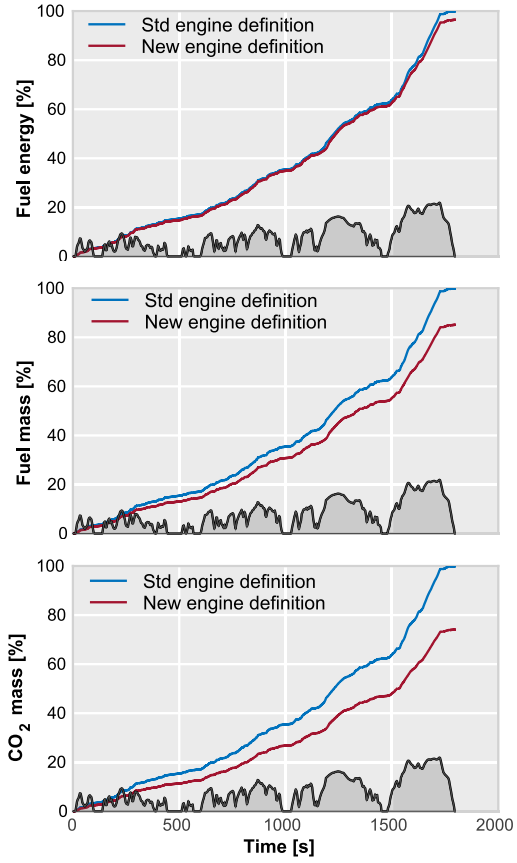

Fig. 19. Power consumption, fuel consumption and CO_2 emissions for the *World Harmonized Light-duty vehicle test Procedure* (WLTP) driving cycle comparing both engine configurations.

main objective of this new engine configuration was to reduce pollutant emissions, especially CO_2. As can be seen in the last graph of Fig. 19, the CO_2 emitted is reduced by about 25% compared to the standard SI engine configuration.

This CO_2 reduction is very promising as it is expected to increase by further optimizing the engine hardware (passive pre-chamber design or matching between the compression ratio and Miller intake opening duration), as well as including other subsystems like turbocharger or VVT, and by a fine-tuning of the engine control strategy.

4. Summary and conclusions

This investigation has addressed an important research gap of the current literature by analyzing the cross-benefits of several technological bricks integrated into a single SI engine, in order to evaluate a futuristic engine architecture for light-duty (passenger car) applications, providing insightful and novel contributions to both the scientific community and the industry. The studied engine definition uses a high compression ratio (15.4:1) to exploit the benefits of CNG and a Miller cycle camshaft in terms of knock mitigation. However, as these strategies have a negative impact on the combustion process itself, an additional solution was evaluated by integrating the passive pre-chamber concept in order to enhance the ignition event. Furthermore, the research methodology adopted for this work has employed a broad combination of experimental activities and 1D through 3D-CFD numerical simulations to understand the underlying physical characteristics of the studied technologies in terms of combustion and in-cylinder fluid dynamics, and apply the acquired knowledge to assess the real performance of the new engine architecture in terms of efficiency, fuel consumption, CO_2 emissions and synergies with EGR dilution.

Thus, the most important findings of the research are presented as follows:

- Few differences were found between the ignition sequence and combustion evolution of gasoline and CNG using the passive pre-chamber concept, at least in un-diluted stoichiometric conditions where the laminar flame speeds of both fuels are relatively high. This gives an interesting degree of freedom to design the engine in order to take advantage of the particular fuel properties of CNG and the accelerated combustion process achieved with the passive pre-chamber, product of the greater flame surface generated with this ignition system.
- The Miller cycle operation deteriorates the fluid-dynamic conditions inside the main chamber (lower levels of turbulence and higher amounts of residual gases); however, the pre-chamber flow conditions are improved with the higher compression ratio of the

new engine architecture, enabling a suitable combustion process in this region which in turn improves the combustion in the main chamber.
- The overall performance of the new engine architecture operating with CNG was improved with respect to the baseline engine, achieving higher levels of efficiency even to those obtained with the reference configuration operating with gasoline. Furthermore, the addition of EGR allows to both achieve higher levels of efficiency in the whole engine map and to extend the load limit of the low-end torque region of the map.
- Finally, from the transient driving cycle simulations, the potential of this new type of engine architectures fueled with CNG and using the passive pre-chamber technology was confirmed. These results showed a remarkable reduction both in fuel consumption (about 15%) and in CO_2 emissions (around 25%), compared to a conventional SI engine definition fueled with gasoline. This was achieved even without performing a dedicated optimization of the complete engine power plant, which is the target of future research activities.

List of symbols/abbreviations

SI: Spark-ignition
CI: Compression-ignition
TJI: Turbulent jet ignition
MC: Main combustion chamber
PC: Pre-chamber
CFD: Computational fluid dynamics
CNG: Compressed Natural Gas
NO_x: Nitrogen oxides
PFI: Port fuel injection
$DOHC$: Double over-head camshaft
CO_2: Carbon dioxide
λ: Relative air-to-fuel equivalence ratio
EGR: Exhaust Gas Recirculation
RON: Research Octane Number
CCV: cycle-to-cycle variability
TDC: Top dead center
IVC: Intake valve closing
ST: Spark timing
CAD: Crankangle degree
$CADaTDC$: Crankangle after the Top dead center
$CADaST$: Crankangle after the Spark timing
HRR: Heat release rate
HR: Heat release
Δp: Pressure difference between the pre-chamber and main chamber
$IMEP$: Indicated mean effective pressure
$\sigma IMEP$: Variability of the IMEP
$ISFC$: Indicated specific fuel consumption
$MAPO$: Maximum amplitude pressure oscillation
COV: Coefficient of variance
$CA50$: Crankangle after 50% of fuel burned
MBT: Maximum Brake Torque
$URANS$: Unsteady Reynolds-averaged Navier Stokes
$ECFM$: Extended Coherent Flamelet Model
TKE: Turbulent kinetic energy

Declaration of competing interest

The authors declare that they have no known competing financial interests or personal relationships that could have appeared to influence the work reported in this paper.

Data availability

Data will be made available on request.

Acknowledgments

The authors want to express their gratitude to CONVERGENT SCIENCE Inc. and Convergent Science GmbH for their kind support for the 0D, 1D and CFD calculations with the CONVERGE software.

The work has been partially supported by the Spanish Ministerio de Ciencia e Innovación through grant number PID2021-12581OB-C21.

References

[1] S. Nalley, A. LaRose, International energy outlook 2021 (IEO2021), 2021.
[2] R. O'Driscoll, M.E. Stettler, N. Molden, T. Oxley, H.M. ApSimon, Real world CO2 and NOx emissions from 149 Euro 5 and 6 diesel, gasoline and hybrid passenger cars, Sci. Total Environ. 621 (2018) 282–290.
[3] Z. Zhongming, L. Linong, Y. Xiaona, Z. Wangqiang, L. Wei, et al., Transport: increasing oil consumption and greenhouse gas emissions hamper EU progress towards environment and climate objectives, 2020.
[4] S. Yu, M. Zheng, Future gasoline engine ignition: A review on advanced concepts, Int. J. Engine Res. 22 (6) (2021) 1743–1775.
[5] E.A.O.A.M. (ACEA), Data on motor vehicle sales in the European union in 2021 and 2022, compiled by ACEA, 2022, URL https://www.acea.auto/files/20220720_PRPC-fuel_Q2-2022_FINAL.xlsx.
[6] S. Cho, C. Song, N. Kim, S. Oh, D. Han, K. Min, Influence of the wall temperatures of the combustion chamber and intake ports on the charge temperature and knock characteristics in a spark-ignited engine, Appl. Therm. Eng. 182 (2021) 116000.
[7] J. Pan, H. Wei, G. Shu, M. Pan, D. Feng, N. Li, LES analysis for auto-ignition induced abnormal combustion based on a downsized SI engine, Appl. Energy 191 (2017) 183–192.
[8] M. Selim, Sensitivity of dual fuel engine combustion and knocking limits to gaseous fuel composition, Energy Convers. Manage. 45 (3) (2004) 411–425.
[9] O. Hijazi, et al., Review of life cycle assessment for biogas production in europe, Renew. Sustain. Energy Rev. 54 (2016) 1291–1300.
[10] A. Shamekhi, et al., Performance and emissions characteristics investigation of a bi-fuel SI engine fuelled by CNG and gasoline, in: ASME Internal Combustion Engine Division Spring Technical Conference, American Society of Mechanical Engineers Digital Collection, 2006, pp. 393–400.
[11] T. Li, et al., The Miller cycle effects on improvement of fuel economy in a highly boosted, high compression ratio, direct-injection gasoline engine: EIVC vs. LIVC, Energy Convers. Manage. 79 (2014) 59–65.
[12] A. Al-Sarkhi, et al., Efficiency of a Miller engine, Appl. Energy 83 (4) (2006) 343–351.
[13] M. Aghahasani, A. Gharehghani, A.M. Andwari, M. Mikulski, J. Könnö, Effect of natural gas direct injection (NGDI) on the performance and knock behavior of an SI engine, Energy Convers. Manage. 269 (2022) 116145.
[14] J. Wang, X. Duan, W. Wang, J. Guan, Y. Li, J. Liu, Effects of the continuous variable valve lift system and Miller cycle strategy on the performance behavior of the lean-burn natural gas spark ignition engine, Fuel 297 (2021) 120762.
[15] K. Xing, H. Huang, X. Guo, Y. Wang, Z. Tu, J. Li, Thermodynamic analysis of improving fuel consumption of natural gas engine by combining Miller cycle with high geometric compression ratio, Energy Convers. Manage. 254 (2022) 115219.
[16] Z. Ran, D. Hariharan, B. Lawler, S. Mamalis, Exploring the potential of ethanol, CNG, and syngas as fuels for lean spark-ignition combustion-an experimental study, Energy 191 (2020) 116520.
[17] Z. Han, Z. Wu, Y. Huang, Y. Shi, W. Liu, Impact of natural gas fuel characteristics on the design and combustion performance of a new light-duty CNG engine, Int. J. Automot. Technol. 22 (2021) 1619–1631.
[18] F. Ma, Y. Wang, J. Wang, S. Ding, Y. Wang, S. Zhao, Effects of combustion phasing, combustion duration, and their cyclic variations on spark-ignition (SI) engine efficiency, Energy Fuels 22 (5) (2008) 3022–3028.
[19] H. Bayraktar, O. Durgun, Development of an empirical correlation for combustion durations in spark ignition engines, Energy Convers. Manage. 45 (9–10) (2004) 1419–1431.
[20] Z. Wang, S. Shuai, Z. Li, W. Yu, A review of energy loss reduction technologies for internal combustion engines to improve brake thermal efficiency, Energies 14 (20) (2021) 6656.
[21] F. Bozza, V. De Bellis, D. Tufano, E. Malfi, C. Müller, K. Habermann, 1D numerical and experimental investigations of an ultralean pre-chamber engine, SAE Int. J. Engines 13 (2) (2020) 159–174.
[22] P. Burkardt, C. Wouters, S. Pischinger, Potential of alcohol fuels in active and passive pre-chamber applications in a passenger car spark-ignition engine, Int. J. Engine Res. (2021) 14680874211053168.
[23] C.E.C. Alvarez, G.E. Couto, V.R. Roso, A.B. Thiriet, R.M. Valle, A review of prechamber ignition systems as lean combustion technology for SI engines, Appl. Therm. Eng. 128 (2018) 107–120.
[24] P. Chinnathambi, B. Thelen, D. Cook, E. Toulson, Performance metrics for fueled and unfueled turbulent jet igniters in a rapid compression machine, Appl. Therm. Eng. 182 (2021) 115893.

[25] W.P. Attard, H. Blaxill, E.K. Anderson, P. Litke, Knock limit extension with a gasoline fueled pre-chamber jet igniter in a modern vehicle powertrain, SAE Int. J. Engines 5 (3) (2012) 1201–1215.

[26] M. Kettner, M. Rothe, A. Velji, U. Spicher, D. Kuhnert, R. Latsch, A new flame jet concept to improve the inflammation of lean burn mixtures in SI engines, SAE Trans. (2005) 1549–1557.

[27] E. Toulson, H.C. Watson, W.P. Attard, The Effects of Hot and Cool EGR with Hydrogen Assisted Jet Ignition, Tech. Rep., SAE Technical Paper, 2007.

[28] S. Posch, H. Winter, J. Zelenka, G. Pirker, A. Wimmer, Development of a tool for the preliminary design of large engine prechambers using machine learning approaches, Appl. Therm. Eng. 191 (2021) 116774.

[29] C. Hu, Z. Zhang, M. Tian, N. Liu, S. Wei, Research on application of asymmetrical pre-chamber in air-assisted direct injection kerosene engine, Appl. Therm. Eng. 204 (2022) 117919.

[30] J. Benajes, R. Novella, J. Gomez-Soriano, P. Martinez-Hernandiz, C. Libert, M. Dabiri, Evaluation of the passive pre-chamber ignition concept for future high compression ratio turbocharged spark-ignition engines, Appl. Energy 248 (2019) 576–588.

[31] G. Xu, Y.M. Wright, M. Schiliro, K. Boulouchos, Characterization of combustion in a gas engine ignited using a small un-scavenged pre-chamber, Int. J. Engine Res. 21 (7) (2020) 1085–1106.

[32] F. Payri, S. Molina, J. Martín, O. Armas, Influence of measurement errors and estimated parameters on combustion diagnosis, Appl. Therm. Eng. (ISSN: 1359-4311) 26 (2) (2006) 226–236, http://dx.doi.org/10.1016/j.applthermaleng.2005.05.006, URL http://www.sciencedirect.com/science/article/pii/S1359431105001560.

[33] C. Guardiola, J. López, J. Martín, D. García-Sarmiento, Semiempirical in-cylinder pressure based model for NOx prediction oriented to control applications, Appl. Therm. Eng. 31 (16) (2011) 3275–3286.

[34] CONVERGE 2.4 Theory Manual, CONVERGENT SCIENCE Inc., 2018.

[35] A. Torregrosa, P. Olmeda, B. Degraeuwe, M. Reyes, A concise wall temperature model for DI diesel engines, Appl. Therm. Eng. 26 (11–12) (2006) 1320–1327.

[36] J. Kim, R. Scarcelli, S. Som, A. Shah, M.S. Biruduganti, D.E. Longman, Numerical investigation of a fueled pre-chamber spark-ignition natural gas engine, Int. J. Engine Res. 23 (9) (2022) 1475–1494.

[37] V. Yakhot, S.A. Orszag, Renormalization group analysis of turbulence. I. Basic theory, J. Sci. Comput. 1 (1) (1986) 3–51.

[38] R. Cant, SB pope, turbulent flows, Cambridge University Press, Cambridge, UK, Combust. Flame 125 (2001) 1361–1362.

[39] F.G.L. Amorim, J.H.M. Ribeiro, M.G.J. Vaz, R.M. Valle, Sensitivity analysis of the air flow inside a single cylinder engine for different turbulence models using CFD, in: Advanced Materials Research, Vol. 1016, Trans Tech Publ, 2014, pp. 624–629.

[40] R.M. Braga, L.M. Reis, L.G. Fonseca, R. Huebner, R.M. Valle, Numerical analysis of the in-cylinder flow field and comparison with experimental data in a single cylinder research engine, Rev. Interdiscip. Pesqui. Engen. 2 (31) (2016) 270–285.

[41] C. Angelberger, T. Poinsot, B. Delhay, Improving Near-Wall Combustion and Wall Heat Transfer Modeling in SI Engine Computations, Tech. Rep., SAE Technical Paper, 1997.

[42] O. Redlich, J.N. Kwong, On the thermodynamics of solutions. V. An equation of state. Fugacities of gaseous solutions, Chem. Rev. 44 (1) (1949) 233–244.

[43] F.E. Marble, J.E. Broadwell, The Coherent Flame Model for Turbulent Chemical Reactions, Tech. Rep., Purdue Univ Lafayette in Project Squidheadquarters, 1977.

[44] P. Boudier, S. Henriot, T. Poinsot, T. Baritaud, A model for turbulent flame ignition and propagation in spark ignition engines, in: Symposium (International) on Combustion, Vol. 24, Elsevier, 1992, pp. 503–510.

[45] O. Colin, A. Benkenida, C. Angelberger, 3D modeling of mixing, ignition and combustion phenomena in highly stratified gasoline engines, Oil Gas Sci. Technol. 58 (1) (2003) 47–62.

[46] O. Colin, A. Benkenida, The 3-zones extended coherent flame model (ECFM3Z) for computing premixed/diffusion combustion, Oil Gas Sci. Technol. 59 (6) (2004) 593–609.

[47] T. Poinsot, D. Veynante, Theoretical and Numerical Combustion, RT Edwards, Inc., 2005.

[48] O. Colin, K. Truffin, A spark ignition model for large eddy simulation based on an FSD transport equation (ISSIM-LES), Proc. Combus. Inst. 33 (2) (2011) 3097–3104.

[49] J. Duclos, O. Colin, (2-25) arc and kernel tracking ignition model for 3D spark-ignition engine calculations ((SI-7) SI engine combustion 7-modeling), in: The Proceedings of the International Symposium on Diagnostics and Modeling of Combustion in Internal Combustion Engines 01.204, The Japan Society of Mechanical Engineers, 2001, p. 46.

[50] J. Benajes, R. Novella, J. Gomez-Soriano, I. Barbery, C. Libert, F. Rampanarivo, M. Dabiri, Computational assessment towards understanding the energy conversion and combustion process of lean mixtures in passive pre-chamber ignited engines, Appl. Therm. Eng. 178 (2020) 115501.

[51] J. Benajes, R. Novella, J. Gomez-Soriano, I. Barbery, C. Libert, Advantages of hydrogen addition in a passive pre-chamber ignited si engine for passenger car applications, Int. J. Energy Res. 45 (9) (2021) 13219–13237.

[52] Y.-D. Liu, M. Jia, M.-Z. Xie, B. Pang, Enhancement on a skeletal kinetic model for primary reference fuel oxidation by using a semidecoupling methodology, Energy Fuels 26 (12) (2012) 7069–7083.

[53] J. Brakora, R.D. Reitz, A Comprehensive Combustion Model for Biodiesel-Fueled Engine Simulations, Tech. Rep., SAE Technical Paper, 2013.

[54] Z. Wang, J.-X. Wang, S.-J. Shuai, Q.-J. Ma, Effects of Spark Ignition and Stratified Charge on Gasoline HCCI Combustion with Direct Injection, Tech. Rep., SAE Technical Paper, 2005.

[55] M. Metghalchi, J.C. Keck, Burning velocities of mixtures of air with methanol, isooctane, and indolene at high pressure and temperature, Combust. Flame 48 (1982) 191–210.

[56] G. Mech, Development and validation of a reduced chemical kinetic mechanism for CFD simulation of combustion in a GCH4/GO2 combustor.

[57] W.K. Metcalfe, S.M. Burke, S.S. Ahmed, H.J. Curran, A hierarchical and comparative kinetic modeling study of C1- C2 hydrocarbon and oxygenated fuels, Int. J. Chem. Kinet. 45 (10) (2013) 638–675.

[58] S. Jerzembeck, N. Peters, P. Pepiot-Desjardins, H. Pitsch, Laminar burning velocities at high pressure for primary reference fuels and gasoline: Experimental and numerical investigation, Combust. Flame 156 (2) (2009) 292–301.

[59] E. Hu, X. Li, X. Meng, Y. Chen, Y. Cheng, Y. Xie, Z. Huang, Laminar flame speeds and ignition delay times of methane–air mixtures at elevated temperatures and pressures, Fuel 158 (2015) 1–10.

[60] R. Novella, J. Gomez-Soriano, I. Barbery, C. Libert, Numerical analysis of the passive pre-chamber ignition concept for light duty applications, Appl. Therm. Eng. (2022) 118610.

[61] J.J. López, R. Novella, J. Gómez-Soriano, P.J. Martinez-Hernandiz, F. Rampanarivo, C. Libert, M. Dabiri, Advantages of the unscavenged pre-chamber ignition system in turbocharged natural gas engines for automotive applications, Energy 218 (2021) 119466.

[62] J. Benajes, R. Novella, J. Gomez-Soriano, P. Martinez-Hernandiz, C. Libert, M. Dabiri, Performance of the passive pre-chamber ignition concept in a spark-ignition engine for passenger car applications, in: Proceedings of the SIA Powertrain Electronics, Paris, France, 2019, pp. 12–13.

[63] R. Novella, J. Pastor, J. Gomez-Soriano, I. Barbery, C. Libert, F. Rampanarivo, C. Panagiotis, M. Dabiri, Experimental and Numerical Analysis of Passive Pre-Chamber Ignition with EGR and Air Dilution for Future Generation Passenger Car Engines, Tech. Rep., SAE Technical Paper, 2020.

[64] D. Siano, M.A. Panza, D. D'Agostino, Knock detection based on MAPO analysis, AR model and discrete wavelet transform applied to the in-cylinder pressure data: results and comparison, SAE Int. J. Engines 8 (1) (2015) 1–13.